J Mater Sci: Mater Electron (2023) 34:1426

Photocatalytic degradation of methylene blue on strontium-doped cobalt ferrite

G. Nandhini[1], S. Kavita[2], T. Pazhanivel[3], and M. K. Shobana[1,*]

[1] Department of Physics, School of Advanced Sciences, Vellore Institute of Technology, Vellore, Tamil Nadu 632014, India
[2] Centre for Automotive Energy Materials, International Advanced Research Centre for Powder Metallurgy and New Materials (ARCI), IIT-M Research Park, Chennai, Tamil Nadu 600113, India
[3] Smart Materials Interface Laboratory, Department of Physics, Periyar University, Salem, Tamil Nadu 636011, India

Received: 6 April 2023
Accepted: 18 June 2023
Published online: 26 June 2023

ABSTRACT

Spinel cobalt ferrite nanoparticles (NPs) have been synthesized using the sol–gel combustion technique with the nominal composition of $Co_{1-x}Sr_xFe_2O_4$ (x = 0.2). The presence of Sr^{2+} ions in $CoFe_2O_4$ nanoparticles exhibits variation in their structural properties with the average crystalline size of 34.07, 36.32, and 35.49 nm when they undergo different heat treatments, labeled as Sr-200, 300, and 500 °C. The formation of a pure phase of $Co_{1-x}Sr_xFe_2O_4$ nanoparticles is identified by Raman spectroscopy. The magnetic behavior of the prepared sample exhibits a change in the magnetic parameter values due to the increase in temperature. The saturation magnetization (M_s), coercivity (H_c), and magnetic anisotropy (k) values have been decreased with an increase in temperature variation from 63.42 to 33.24 emu/g, 1119.7 to 1034.4 O_e, and 73.9 to 35.8 $emuO_eg^{-1}$, respectively. Thus, the highest M_s value is observed for the sample treated at 200 °C. The prepared $Co_{1-x}Sr_xFe_2O_4$ NPs are used to remove the methylene blue (MB) dye and exhibited degradation efficiency with the highest value of 72% for the sample treated at 500 °C for 45 min. In this report, we highlight that the divalent (Sr) doped cobalt ferrite samples are encouraged for magnetic storage and wastewater management applications.

1 Introduction

The utilization of ferrites in the field of nanoscience and technology grasp the attention of several researchers owing to its outstanding properties in various applications like biomedicine [1], magnetic storage [2], miniaturized antennas in mobile devices [3], Solid Oxide Fuel Cells (SOFCs) [4], Solid Oxide Electrolyzer Cells (SOECs) [5], microelectronics [6], Radio-Frequency (RF) applications [7], wastewater management [8–10], supercapacitors [11], electrical transport [12], and gas sensors [13], etc. Ferrites are more intriguing because of their normal and inverse forms of spinel structure, out of garnet, and hexagonal structures [14, 15]. Among the family of spinel ferrites, cobalt ferrite has been extensively studied

Address correspondence to E-mail: mkshobana@gmail.com

https://doi.org/10.1007/s10854-023-10866-0

because of its high Curie point (793 K), large Kerr effect, high H_c, moderate M_s, large magneto-crystalline anisotropy (k), high magnetostrictive coefficient, electrical insulation, chemical stability, wear resistance, and mechanical hardness. It is a well-known photomagnetic material that shows an interesting light-induced coercivity change. In bulk form, it exhibits the ferrimagnetic behavior with T_c around 790 K and partially crystallizes to inverse spinel structure with Fd-3 m space group.

The general representation can be written as $(Co_{1-x}Fe_x)$ $[Co_xFe_{2-x}]$ O_4, in which $(Co_{1-x}Fe_x)$ represents the A-site (tetrahedral) and $[Co_xFe_{2-x}]$ represents the B-site (octahedral) coordination. Here, "x" is the degree of inversion and the fraction of Fe^{3+} cations that are present in the A-sites. The normal and inverse spinel structures are represented by the value of $x = 0$ and 1, respectively, and also depend on the sample's thermal history [16]. Thus, cobalt ferrite NPs exhibit mixed spinel structure and not in inverse spinel form. This is one of the reasons for its reduced saturation magnetization [17].

Cobalt ferrite ($CoFe_2O_4$) is known for its versatility in applications like medical diagnostics, information storage, magnetic refrigeration, ferrofluid technology, and magneto-mechanical devices. The strain and magnetostriction depend mainly on magneto-crystalline anisotropy (k), in which it is determined by Co^{2+} spin–orbit coupling at the B-site. Also, in the octahedral site, the crystal field symmetry of the subsequent nearest neighbor cation is expected to reduce. Similarly, Fe^{3+} is substituted for tetravalent cation with preferential tetrahedral or octahedral coordination [18]. During the synthesis, this large number of empty sites allows cations to migrate between interstitial sites [19]. To tailor the performance of the material, it is necessary to ascertain the structural parameters and cation site occupancies because the cation allocation in the lattice sites is highly dependent on the material preparation [20].

Rare-earth doping of trivalent cations in spinel ferrites has been acknowledged as a potential candidate to enhance electrical and magnetic properties. This type of doping induces the trivalent Fe-cations and rare-earth cations (RE^{3+}–Fe^{3+}) interactions and trivalent Fe^{3+}–Fe^{3+} interactions, which are influenced by the antiferromagnetic super-exchange interactions. In memory storage sectors, the doping of non-magnetic Sr ions in cobalt ferrite has a significant effect on its properties towards memory storage applications [21]. Strontium, being one of the best alkali earth metals with an atomic radius of 219 p.m. suppresses the structural changes, when doped with cobalt ferrite (atomic radius—152 p.m.) because of its atomic size difference [22, 23].

The utilization of cobalt ferrite in scientific research indicates that it has excellent photocatalytic behavior with prospective uses in medicine and the environment. Ahmed et al. synthesized capsaicin-coated cobalt ferrite nanoparticles and pure $CoFe_2O_4$ using fuchsine basic degradation at 94.6% equilibrium. Additionally, they ensure that the produced nanoparticles will function as effective antibacterial agents against both Gram-negative as well as Gram-positive bacteria [24]. 97% of the maximum methylene blue dye disappeared after 180 min of irradiation when polyester fabric was decorated with cobalt ferrite using the co-precipitation method. According to Zarezadeh et al., the active species trapping investigations showed that the photocatalytic degradation mechanism was more effective with hydroxyl radicals as the active species [25].

Due to the greater ionic radii of different rare-earth metal ions in cobalt ferrite nanoparticles, a noticeable change in their structural, magnetic, and optical properties is observed. In this case, the bandgap values will be reduced and that facilitates the transfer of photo-generated holes and electrons. Similarly, to this, Dhiman et al. created a variety of rare-earth doped cobalt ferrite nanoparticles, with Nd doping displaying the best photocatalytic behavior and exhibiting about 9 times the photocatalytic activity of pure cobalt ferrite nanoparticles [26]. There have been various reports of rare earth metal ions like Sm^{3+}, Ce^{4+}, Dy^{3+}, Nd^{3+}, Eu^{3+}, La^{3+}, etc. [27–30]. Consequently, Sr^{2+} metal ions with cobalt ferrite for photocatalytic application have not been reported according to our knowledge. As a result, the current work describes the development of a novel material for photocatalytic activity with a higher degradation percentage. Application-focused projects will also be taken into consideration for our future efforts.

Strontium cobalt iron oxide ceramics provide favorable properties like low-temperature coefficient, high radiation efficiency, and better chemical stability for applications like radiation systems and miniaturized antenna designs [31]. Also, compared to other alkaline earth metals like calcium and barium, strontium is an adequate candidate for magnetic storage and water purification systems [32]. As there

are several experimental techniques to synthesize MNPs, one of the encouraging methods is the sol–gel combustion method, due to its low annealing temperature, lesser time, and the synthesis of NPs at a lower cost. Hence, the doping of Sr ions in cobalt ferrite would tailor the better structural, optical, magnetic, and photocatalytic properties [33].

2 Experimental method

2.1 Sample preparation

The nanocrystalline ferrite samples have been prepared using analytical grade cobalt nitrate (99.99% purity, Sigma-Aldrich Co., USA), strontium nitrate (99.99% purity, Sigma-Aldrich Co., USA), iron nitrate (99.99% purity, Sigma-Aldrich Co., USA), and citric acid (99.99% purity, Sigma-Aldrich Co., USA). The synthesis procedure is same as reported in our previous work by sol–gel combustion method with the chelating agent as polyvinyl alcohol (PVA) [22]. The stoichiometric amounts of nitrates are determined according to the reducing and oxidizing valences of the components from the concepts of chemistry. For the synthesis, molarity ratios of metal precursors powders, PVA, and citric acid are dissolved in DI water and stirred well to make it a homogeneous solution. After then, ammonia is added as a precipitating agent, to obtain a clear transparent solution. In a water bath, the resulting solution is heated at 80 °C. Further, it is heat treated at 150 °C and the resultant product is finely milled. Finally, the samples are annealed at 200, 300, and 500 °C, and the final products obtained are labeled as Sr-200, Sr-300, and Sr-500 °C.

2.2 Photocatalytic activity

The photocatalytic degradation activity of the prepared nanocomposites was investigated by degrading methylene blue dye (MB) in the presence of UV–visible light. In a typical procedure, 100 mg of the catalysts was dispersed in a 100 mL aqueous solution of MB (10 mg L^{-1}). After the exposure to light, the absorbance of MB dye was observed with a UV–Visible spectrophotometer at regular time intervals. A UV–visible spectrometer was used to measure the concentration of the MB solution at its characteristic absorption peak of 664 nm.

2.3 Materials characterization

The prepared nano ferrite samples are structurally characterized by X-ray diffraction (XRD) using Bruker D8 Advance X-ray diffractometer with Cu K alpha radiation (1.54056 Å). The morphology of the sample was investigated by field emission scanning electron microscopy (FE-SEM) from M/S Zeiss Merlin. Raman analysis was used to observe the atomic structure of the nano ferrites using BRUKER RFS. The magnetic studies were carried out by a vibrating sample magnetometer (VSM), Quantum Design, Dynacool-9 T. Also, the degradation efficiencies of the nano ferrites were calculated by UV–Visible spectrophotometer using UV-SHIMADZU 3600.

3 Results and discussion

The XRD patterns of strontium-doped cobalt nano ferrites reveal that the nanoparticles have spinel structure, and no secondary phases were observed with increasing annealing temperatures. It confirms that the doped Sr^{2+} ions are placed in the $CoFe_2O_4$ lattices. The peak matches with the equivalent reflection planes such as (220), (311), (400), (422), (511), (440), and (533) of ICDD (# 022-1086) indicating a cubic single-phase structure. The doping of strontium in cobalt ferrite results in a transition of space group Pm-3 m from Fd-3 m [34, 35]. The samples are heat treated at 200, 300, and 500 °C with an average crystalline size (D) of 34.07, 36.32, and 35.49 nm, respectively (Fig. 1).

The increase in average crystalline size is due to the increase in annealing temperature and agglomeration behavior of ferrites. Further, the crystalline temperature of the prepared material is observed as 400 °C. Thus, it tends to break the bonds of the material with increase in temperature (< 400 °C) and results with the decrease in crystalline size from 36.32 to 35.49 nm [23, 36]. As the lattice parameters and crystalline size depend on each other, it increases with an increase in annealing temperature and decreases with the breakdown of material bonds. When some Co^{2+} ions are replaced by Sr^{2+} ions in $CoFe_2O_4$, the increase or decrease of lattice parameters would depend upon two effects namely: the large size (ionic radii) of Sr^{2+} tries to increase or decrease the lattice parameter and the strain formed by its substitution in the cell, respectively [19, 31]. The presence of Sr^{2+} ions in

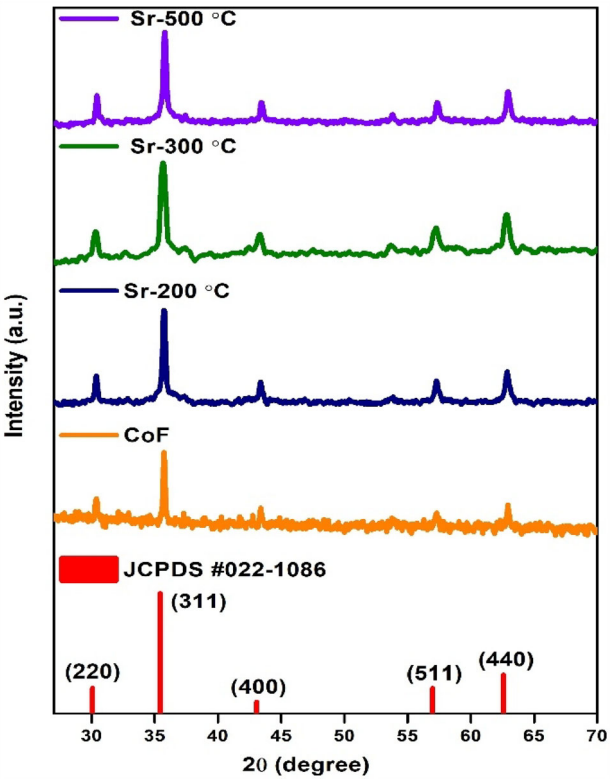

Fig. 1 X-ray diffraction pattern of pure Cobalt ferrite (CoF) and doped ($Co_{0.8}Sr_{0.2}Fe_2O_4$) nanoparticles at 200, 300, and 500 °C

cobalt ferrite is confirmed by the XPS measurements reported in our previous article [22].

The molar mass and the lattice constant of the prepared samples have been interlinked to the parameter namely X-ray density (ρ_x). The obtained X-ray density values have been shown in Table 1, which are inversely proportional to the average crystalline size. The lattice parameters and the average crystalline size of the nanoparticle would depend on the ionic radii and the temperature variations of the material. The appropriate distance between the tetrahedral (L_A) and octahedral sites (L_B) of magnetic ions is termed hopping length, which plays a significant role in determining the physical properties of the ferrites [37, 38]. All the above parameters such as average crystalline size [39], interplanar spacing [40], lattice constant [41], unit cell volume [42], hopping length [43], and the X-ray density [42] are calculated from the equations given in our previous work [21]. The variation of all the parameters (crystalline size, lattice constants, x-ray density, hopping length) with temperature variation is illustrated in Figs. 2 and 3.

The morphology of the prepared sample is investigated through field emission scanning electron microscopy (FE-SEM). The typical cross-sectional micrographs of $Co_{0.8}Sr_{0.2}Fe_2O_4$ nanoparticles is shown in Fig. 4. It is evident that the doping process has an impact in the grain morphologies and boundaries [44]. Pure cobalt ferrite nanoparticles have well-agglomerated irregular structures and non-uniform diameters at a resolution of 300 nm. Besides, Sr ions doped cobalt ferrite nanoparticles at 300 nm resolution exhibits the formation of agglomerated nano-plate like structures. The agglomeration of nanoparticles resulting from the interaction of magnetic nanoparticles induces a variation in the average crystalline size. This may also be a result of its surface tension.

The phase purity of the prepared $Co_{0.8}Sr_{0.2}Fe_2O_4$ samples has been analyzed using Raman spectroscopy at room temperature as shown in Fig. 5. Further, the insights into the atomic structure of the nanoparticles have been determined by this powerful technique. The peaks obtained in the spectroscopy can be deconvoluted into individual Lorentzian peaks [45, 46]. In accordance with the group theory analysis, the spinel structure of the phonon modes can be predicted as follows;

$$A_{1g} + E_g + T_{1g} + 3T_{2g} + 2A_{2u} + 2E_u + 4T_{1u} + 2T_{2u}.$$

Together with the 5 Raman active modes (A_{1g} + E_g + $3T_{2g}$), there are 39 normal modes, including the 4 IR active modes (T_{1u}) for spinel structure ferrites. These modes were determined by the dipole moments of oxygen anion, and the A and B-site ions of the spinel ferrites. The Raman modes (A_{1g}, E_g, T_{2g}) were due to the symmetric stretching, symmetric bonding, and asymmetric stretching of O^{2-}, respectively. The observed Raman modes for $Co_{0.8}Sr_{0.2}Fe_2O_4$ samples at different temperatures are revealed in Table 2 [22]. The A_{1g} (1) and A_{1g} (2) modes at 680 cm^{-1} and 613 cm^{-1} wavenumber regions reflects the tetrahedral site (Fe–O and M–O) bonds for stretching vibrations. At lower frequencies, the wavenumber regions like ~ 570, ~ 467, ~ 304, and ~ 202 cm^{-1} have been representing the E_g and T_{2g} Raman modes of asymmetric stretching vibrations. The Raman modes correspond to the modes of octahedral (B-site) and tetrahedral (A-site) in their sublattice with wavenumber regions above and below 600 cm^{-1}, respectively [47]. Further, minor

Table 1 Outline of crystalline size, lattice constant, cell volume, interplanar spacing, hopping length, and X-ray density of $Co_{0.8}Sr_{0.2}Fe_2O_4$ sample annealed at three different temperatures (200, 300, 500 °C)

Sample name ($Co_{0.8}Sr_{0.2}Fe_2O_4$)	Crystalline size (D) (nm)	Lattice constant (a) (Å)	Unit cell volume (V) (Å^3)	Interplanar spacing (d) (Å)	L_A (Å)	L_B (Å)	X-ray density (ρ_x) (g/cm^3)
Sr-200	34.072	8.331	578.27	2.285	3.607	2.945	5.522
Sr-300	36.327	8.343	580.81	2.288	3.612	2.949	5.497
Sr-500	35.499	8.322	576.44	2.282	3.603	2.941	5.540

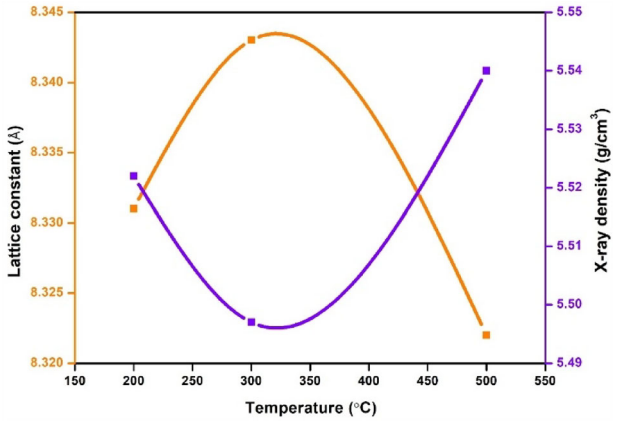

Fig. 2 Variation in Lattice constants and X-ray density with increase in temperature (°C)

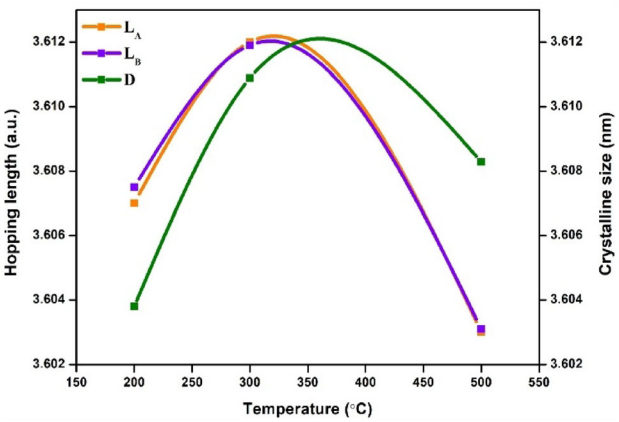

Fig. 3 Variation in Hopping length (L_A and L_B) of tetrahedral and octahedral sites and Crystalline size (D) with increase in temperature (°C)

shifts observe with respect to the temperature treatment of the prepared $Co_{0.8}Sr_{0.2}Fe_2O_4$ samples. It is also a reason for the cations to relocate and increase the crystalline size with reference to the XRD spectrum.

The site preference through crystal field stabilization energy (CFSE) for cations is strongly influenced by its magnetic properties between the octahedral and tetrahedral sites in the spinel lattice [16, 19]. Also, it depends on both intrinsic and extrinsic properties like particle size, chemical composition, deformation, grain sizes, lattice strain, porosity, and density. The exchange interaction between the magnetic ions is of three types namely AA, BB, and AB interactions resting on the sublattices of ferrites. Here, AB super-exchange interactions are attributed to remanent magnetization behavior. Thus, the difference between the two sublattices gives the net magnetic moment ($n_B = M_B - M_A$), according to the Néel model [20, 48]. Where "M_B and M_A" represent the B and A sublattice. By Neel's sublattice theory, the distribution of cations is formulated as, $(Fe)_A[Co_{1-x}Sr_xFe]_BO_4$. Also, the cationic distributions perform a vital role in deciding the difference in A and B site moments. It also determines the strength and the orientation of the prepared nano ferrite sample with the above-given relation. The magnetic moment experimental values [21] were similar to the calculated theoretical magnetic moment values, which decrease with respect to the decrease in saturation magnetization values (M_s) [49].

The hysteresis loop measurements for $Co_{0.8}Sr_{0.2}Fe_2O_4$ (Sr-200, Sr-300, and Sr-500 °C) samples are shown in Fig. 6. It is evident that the saturation magnetization values have been decreasing from 63.42 to 33.24 emu/g with the increase in heat treatment temperature. It is because of two main reasons: the non-alignment of magnetic moments due to the increase in thermal energy and the incorporation of non-magnetic Sr atom in the magnetic network (Fe–O). The strontium ions have 2+ valence electrons and higher ionic radii (Sr^{2+}-126 pm, Co^{2+}-72 pm), which is also a reason for the decrease in M_s values. Also, the behavior of saturation was influenced by the temperature effect [50]. Thus, in relation to the M_s values, the coercivity (H_c) and remanent magnetization (M_r) values are decreasing linearly from 1119.7 to

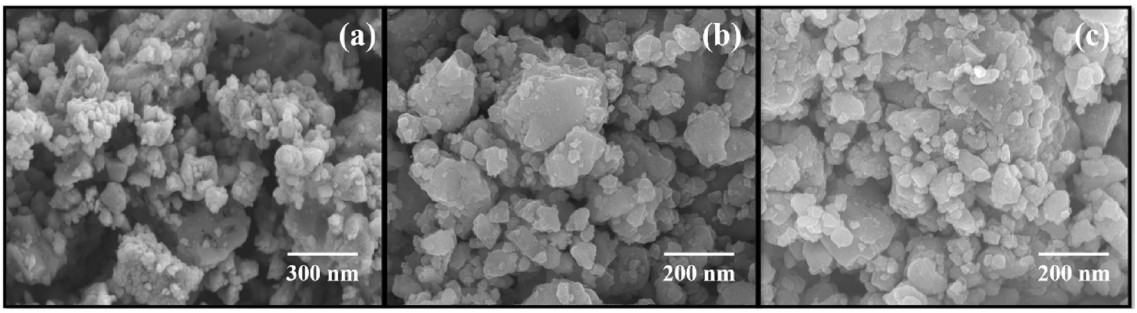

Fig. 4 FE-SEM micrographs of **a** pure cobalt ferrite **b** $Co_{0.8}Sr_{0.2}Fe_2O_4$ @ 200 °C **c** $Co_{0.8}Sr_{0.2}Fe_2O_4$ @ 300 °C

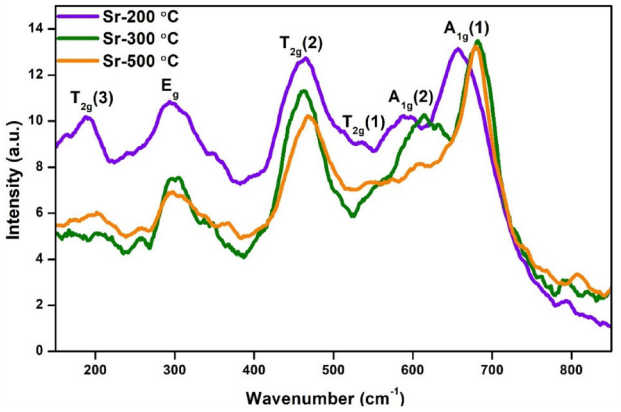

Fig. 5 Raman spectroscopy of $Co_{0.8}Sr_{0.2}Fe_2O_4$ NPs

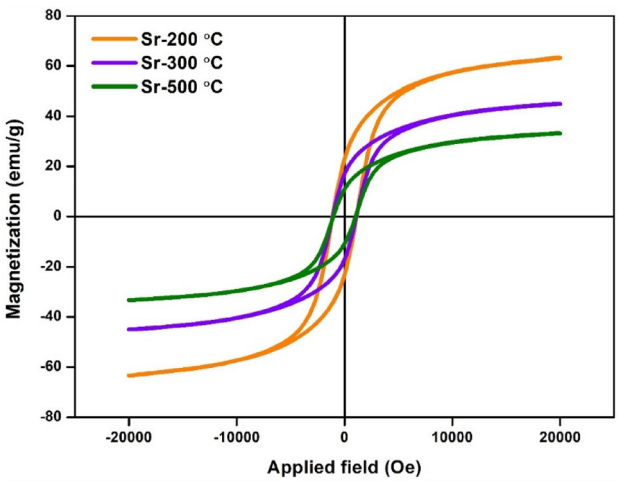

Fig. 6 Hysteresis loop of $Co_{0.8}Sr_{0.2}Fe_2O_4$ NPs

1034.4 Oe and 23.02 to 10.87 emu/g, respectively. At interfaces, the pinning of the magnetic moments is related to a high H_c value and the decrease in coercivity values denotes the crossover from hard to soft ferrite. A significant parameter namely "loop squareness ratio (M_r/M_s)" determines the uniaxial grains that are randomly oriented and are a measure of nearest easy axis magnetization. If the value of the ratio is equal to 0.5, it exhibits superparamagnetic behavior. As the exhibited squareness ratio values are below 0.5, the sample exhibit ferromagnetic nature.

Magnetic anisotropy has been analyzed to determine the magnetic properties by its crystallographic directions using the following formula (Eq. 1). It is noticed that the decrease in magnetic anisotropy constant (k) is due to the addition of non-magnetic material (Sr^{2-}) and the decrease in exchange interaction of Co^{2+} ions [19]. The variation of saturation magnetization and magnetic anisotropy with the increase in temperature is shown in Fig. 7 [50–52].

$$k = \frac{H_c \times M_s}{0.96} \quad (1)$$

The magnetic moment is a behavior of AB superexchange interactions, which results in decreased values, confirming that it is analogous to the saturation magnetization values. Thus, the investigation of nano ferrite sample ($Co_{0.8}Sr_{0.2}Fe_2O_4$) reveals the semi-hard magnetic properties that can be used for magnetic storage applications and in recording systems

Table 2 Temperature dependent raman modes of $Co_{1-x}Sr_xFe_2O_4$ samples

Sample name ($Co_{0.8}Sr_{0.2}Fe_2O_4$)	Raman peak (cm^{-1})					
	A_{1g} (1)	A_{1g} (2)	T_{2g} (1)	T_{2g} (2)	E_g	T_{2g} (3)
Sr-200	658	588	569	463	293	189
Sr-300	680	613	550	462	304	200
Sr-500	679	609	570	467	296	202

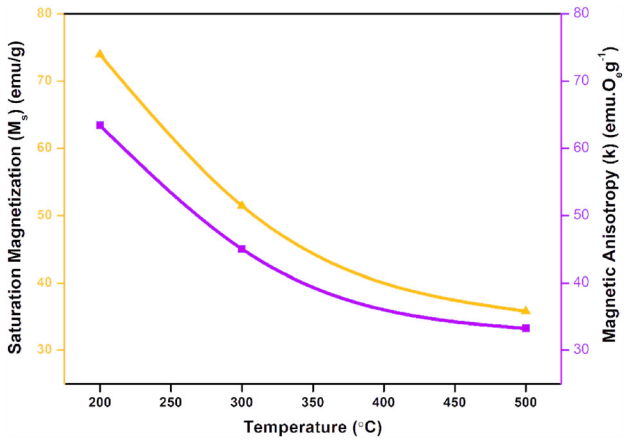

Fig. 7 Variation of M_s and k as a function of temperature (°C)

due to its high coercivity values [33, 53]. All the above-mentioned quantities are mentioned in Table 3.

Magnetic materials like nano ferrites have a suitable reusability property, which is challenging for photocatalytic activity. This activity for the $Co_{0.8}Sr_{0.2}Fe_2O_4$ sample has been analyzed by the degradation of methylene blue (MB) dye for about 45 min. Figure 8 gives the UV–Vis absorption graph of methylene blue dye + $Co_{0.8}Sr_{0.2}Fe_2O_4$ NPs for different irradiation times (from 0 to 45 min) [22, 53, 54]. The fundamental absorbance peak at 663 nm and a small shoulder peak at 610 nm is observed. There is no blue or red shift indicating the existence of any photochemical reaction during the methylene blue degradation, and the color changes from blue to colorless. In this process, reactive species like hydroxyl radicals or superoxide radicals are majorly responsible for the degradation of organic compounds [55, 56].

The mechanism of photocatalysis indicates that the electron moves from the valence band (VB) to the conduction band (CB) and exhibits a hole in the valence band. Further, the reaction with the water molecules produces radicals that degrade the methylene blue dye. The effect of dye concentration, adsorbent dose, contact time, and pH are the factors that affect the photocatalytic degradation of the MB dye. The most significant parameter was the dye concentration, in which the degradation efficiency decreases with the increase in its concentration. It makes the molecules unreached on the catalyst's surface and results in a decreased degradation percentage [57]. Another important parameter was the effect of pH, in which the degradation percentage increases when the pH was below 9. It decreases with the increase in pH above 9, which was due to the oxygen formation anions between the O^{2+} molecules and the photocatalyst electrons [54]. To prevent acidic conditions, we choose the pH level of 6–7 as an optimum condition. This is because methylene blue is negatively charged in an acidic medium, whereas Sr^{3+} nanohybrids are positively charged below pH 9. Further in the basic medium, the photocatalytic activity decreased due to the increase of the electrostatic repulsion between photocatalysts.

Another important factor for the photocatalytic degradation of ferrite magnetic nanoparticles is photo-Fenton catalytic activity [58]. The main mechanism to degrade the MB dye under light irradiation is explained with a redox-cyclic steps,

$$Sr^{2+} + H_2O_2 \rightarrow Sr^{3+} + OH^{\cdot} + OH^{-},$$

$$OH + Sr^{2+} \rightarrow Sr^{3+} + OH^{-},$$

$$Sr^{3+} + H_2O_2 \rightarrow Sr - OOH^{2+} + H^{+},$$

$$Sr - OOH^{2+} \rightarrow HO_2^{\cdot} + Sr^{2+},$$

Table 3 Parameters to determine the magnetic properties of $Co_{1-x}Sr_xFe_2O_4$

Sample name ($Co_{0.8}Sr_{0.2}Fe_2O_4$)	Saturation magnetization M_s (emu/g)	Coercivity H_c (Oe)	Remanent magnetization M_r (emu/g)	Loop squareness ratio (M_r/M_s)	Magnetic moment (n_B) (μ_B) (Experimental value)	Magnetic moment (n_B) (μ_B) (theoretical value)	Magnetic anisotropy ($K \times 10^3$) (emu. $O_e g^{-1}$)
Sr-200	63.420	1119.7	23.023	0.3630	2.729	2.964	73.97
Sr-300	45.052	1097.2	16.978	0.3768	1.939	2.964	51.49
Sr-500	33.243	1034.4	10.878	0.3272	1.431	2.964	35.82

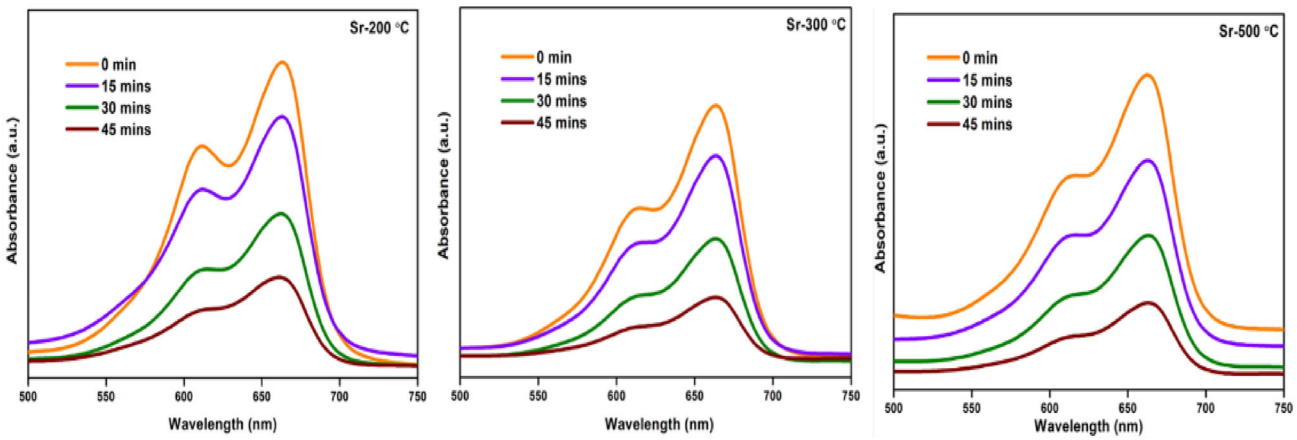

Fig. 8 Photocatalytic degradation of $Co_{0.8}Sr_{0.2}Fe_2O_4$ nanoparticles

$$Sr^{2+} + HO_2^{\cdot} \rightarrow Sr^{2+} + O_2 + H^+,$$

$$Sr^{3+} + HO_2^{\cdot} \rightarrow Fe^{2+} + O_2 + H^+,$$

$$OH^{\cdot} + H_2O_2 \rightarrow H_2O + HO_2^{\cdot}.$$

Figure 9 shows the percentage degradation vs time irradiation plots, in which the catalytic performance has increased with the increase in temperature. Previous articles report that the octahedral sites were surface exposed sites that enhance the photocatalytic behavior while tetrahedral sites are catalytically idle. The presence of Sr^{2+} ions (larger ions) than the iron cations in the octahedral sites makes the photocatalytic behavior active and an excellent degradation pollutant. Hence, by increasing the annealing temperature, the percentage of degradation efficiency is increased and is calculated by the following Eq. 2 [59]. Thus, the $Co_{0.8}Sr_{0.2}Fe_2O_4$ (Sr-500 °C) nanoparticles with methylene blue dye resulted in the catalytic performance of about 72.32% under irradiation time for 45 min, which can be used for wastewater treatment, clean energy, and as a photocatalyst.

$$D(\%) = \frac{C_0 - C}{C_0} \times 100. \quad (2)$$

The annealing temperature strongly influences the photocatalytic degradation of dye using nanomaterial catalysts. Nanomaterials exhibit different charges depending on the temperature, affecting their photocatalytic activity. The optimized temperature range for effective degradation is typically 300–500 °C. The material at its lower temperature (300 °C) attracts dye molecules to the positively charged catalyst surface, reducing the recombination of charge carriers and degradation efficiency. Conversely, the material at

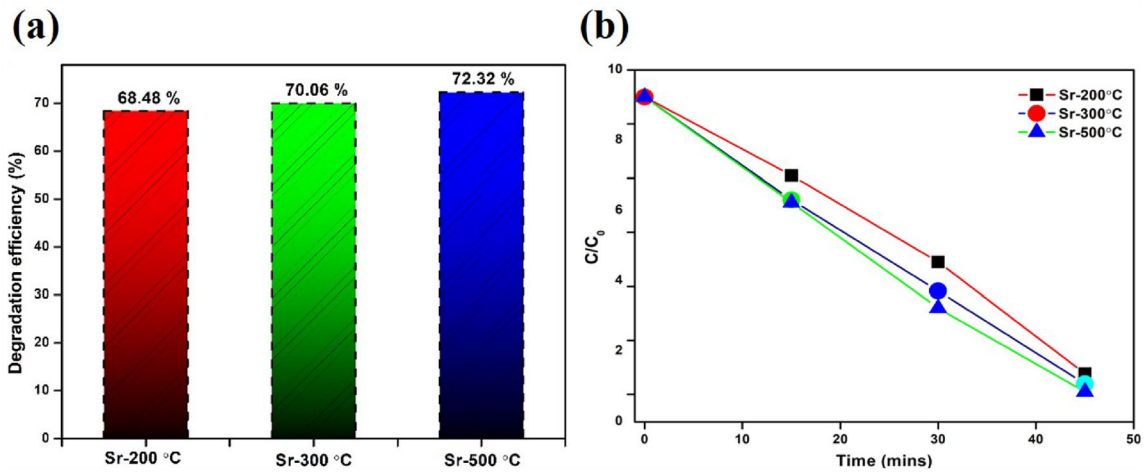

Fig. 9 **a** Degradation efficiency and **b** C/C_0 plot for $Co_{0.8}Sr_{0.2}Fe_2O_4$ nanoparticles

the higher temperature of 500 °C repels negatively charged dye molecules, decreasing their adsorption and increasing photocatalytic activity. Further, charge carrier mobility, auto-generation of oxidizing species (hydroxyl radicals), and increased number of active sites increases the rate reaction at elevated temperatures. Hence, it can result with hydrolysis and the formation of degradation-resistant products. Thus, optimizing the temperature is crucial for efficient photocatalytic degradation using nanomaterial catalysts [60, 61]. Hence, there are no other reports for the photocatalytic properties of strontium-doped cobalt ferrite nanoparticles. Consequently, it is the best degradation efficiency reported so far for this prepared nano ferrite material.

4 Conclusion

Sr-doped $CoFe_2O_4$ NPs are prepared through the sol–gel combustion technique under different annealing temperatures like 200, 300, and 500 °C. XRD confirms the average crystalline sizes of about 34, 36, and 35 nm according to the relative temperature treatments. The variation in the crystalline size is due to the increase in annealing temperature and elevated temperature across its crystalline temperature. The stretching and vibrations in the Raman spectroscopy exhibit the pure form of the synthesized $Co_{1-x}Sr_xFe_2O_4$ NPs. Magnetic illustrations reveal that the increase in the temperature treatments increases the saturation magnetization, coercivity, retentivity, magnetic anisotropy, etc. The maximum saturation magnetization is obtained as 63.420 emu/g, which can act as a strong applicator in magnetic storage devices. Further, the photocatalytic analysis with methylene blue dye exhibits the highest degradation percentage which is not reported to date for the synthesized $Co_{0.8}Sr_{0.2}Fe_2O_4$ NPs. The value of the highest degradation efficiency for the irradiation time of 45 min is calculated to be 72.32%. This maximum efficiency of the strontium-doped cobalt ferrite would be an efficient photocatalyst and also an effective material in wastewater management devices.

Author contributions

GN: writing—original draft, review & editing. SK: formal analysis, investigation. TP: formal analysis, investigation. MKS: conceptualization, methodology, writing—review & editing, validation.

Funding

The authors are grateful to Vellore Institute of Technology for providing "VIT SEED GRANT-2022" for carrying out this research work.

Data availability

The data will be made available on reasonable request.

Declarations

Conflict of interest The authors declare that they have no known competing financial interests or personal relationship that could have appeared to influence the work reported in this paper.

References

1. G. Nandhini, M.K. Shobana, Role of ferrite nanoparticles in hyperthermia applications. J. Magn. Magn. Mater. **552**, 169236 (2022). https://doi.org/10.1016/j.jmmm.2022.169236
2. S. Khan, B. Ali, M. Salman et al., Spinel M0.5Zn0.5Fe2O4 (M = Ni Co, and Cu) ferrites for energy storage applications: dielectric, magnetic and electrochemical properties. Ceram. Int. (2022). https://doi.org/10.1016/j.ceramint.2022.05.290
3. Y. Li, Q. Feng, Z. Zheng, A compact dual-band planar antenna loaded with magneto dielectric ferrite. Appl. Comput. Electromagn. Soc. J. **36**, 1579–1585 (2021). https://doi.org/10.1305/2021.ACES.J.361209
4. T. Solid, O. Fuel, A. Fuzamy et al (2022) Electrochemical evaluation of nickel oxide addition toward lanthanum strontium cobalt ferrite cathode for intermediate
5. K. Cook, J. Wrubel, Z. Ma et al., Modeling electrokinetics of oxygen electrodes in solid oxide electrolyzer cells. J. Electrochem. Soc. **168**, 114510 (2021). https://doi.org/10.1149/1945-7111/ac35fc
6. B. Sapkota, M.T. Hasan, A. Martin et al., Fabrication and magnetoelectric investigation of flexible PVDF-TrFE/cobalt

ferrite nanocomposite films. Mater. Res. Express (2022). https://doi.org/10.1088/2053-1591/ac6151
7. M. Arya, M.N. Gandhi, S.S. Prabhu et al., Nickel-cobalt-zinc ferrite nanoparticles for radio-frequency/terahertz frequency-selective surface application. IET Nanodielectr **4**, 98–106 (2021). https://doi.org/10.1049/nde2.12004
8. B. Verma, C. Balomajumder, Synthesis of magnetic nickel ferrites nanocomposites: an advanced remediation of electroplating wastewater. J. Taiwan Inst. Chem. Eng. **112**, 106–115 (2020). https://doi.org/10.1016/j.jtice.2020.07.006
9. J. Kang, Y. Tang, M. Wang et al., The enhanced peroxymonosulfate-assisted photocatalytic degradation of tetracycline under visible light by g-C3N4/Na-BiVO4heterojunction catalyst and its mechanism. J. Environ. Chem. Eng. **9**, 105524 (2021). https://doi.org/10.1016/j.jece.2021.105524
10. S. Li, Y. Tang, M. Wang et al., NiO/g-C3N4 2D/2D heterojunction catalyst as efficient peroxymonosulfate activators toward tetracycline degradation: characterization, performance and mechanism. J. Alloys Compd. **880**, 160547 (2021). https://doi.org/10.1016/j.jallcom.2021.160547
11. B.M. Al-Maswari, N. Al-Zaqri, J. Ahmed et al., Nanomagnetic strontium ferrite nitrogen doped carbon (SrFe2O4-NC): synthesis, characterization and excellent supercapacitor performance. J. Energy Storage **52**, 104821 (2022). https://doi.org/10.1016/j.est.2022.104821
12. Y. Wang, H. Wang, W. Tan, D. Huo, Magnetization reversal, critical behavior, and magnetocaloric effect in NdMnO3: the role of magnetic ordering of Nd and Mn moments. J. Appl. Phys. (2022). https://doi.org/10.1063/5.0124002
13. A. Šutka, K.A. Gross, Spinel ferrite oxide semiconductor gas sensors. Sens. Actuators B Chem. **222**, 95–105 (2016). https://doi.org/10.1016/j.snb.2015.08.027
14. V.G. Ivanov, M.V. Abrashev, M.N. Iliev et al., Short-range B -site ordering in the inverse spinel ferrite NiFe 2O4. Phys. Rev. B **82**, 1–10 (2010). https://doi.org/10.1103/PhysRevB.82.024104
15. Z. Szotek, W.M. Temmerman, D. Ködderitzsch et al., Electronic structures of normal and inverse spinel ferrites from first principles. Phys. Rev. B **74**, 1–12 (2006). https://doi.org/10.1103/PhysRevB.74.174431
16. A. Franco, E. Silva, High temperature magnetic properties of cobalt ferrite nanoparticles. Appl. Phys. Lett. **96**, 2010–2013 (2010). https://doi.org/10.1063/1.3422478
17. F. Nakagomi, S.W. Da Silva, V.K. Garg et al., The influence of cobalt population on the structural properties of Cox Fe3–x O4. J. Appl. Phys. **101**, 4–7 (2007). https://doi.org/10.1063/1.2712821
18. V.R. Monaji, D. Das, Influence of Zr doping on the structural, magnetic and magnetoelastic properties of cobalt-ferrites. J. Alloys Compd. **634**, 99–103 (2015). https://doi.org/10.1016/j.jallcom.2015.02.084
19. A.C. Lima, A.P.S. Peres, J.H. Araújo et al., The effect of Sr2+ on the structure and magnetic properties of nanocrystalline cobalt ferrite. Mater. Lett. **145**, 56–58 (2015). https://doi.org/10.1016/j.matlet.2015.01.066
20. S. Chakrabarty, A. Dutta, M. Pal, Enhanced magnetic properties of doped cobalt ferrite nanoparticles by virtue of cation distribution. J. Alloys Compd. **625**, 216–223 (2015). https://doi.org/10.1016/j.jallcom.2014.10.179
21. M.K. Shobana, G. Nandhini, S. Kavita et al., Photocatalytic and magnetic properties of Mg substituted cobalt ferrite. Mater. Sci. Eng. B Solid-State Mater. Adv. Technol. **286**, 116030 (2022). https://doi.org/10.1016/j.mseb.2022.116030
22. M.K. Shobana, H. Park, H. Choe, Effect of strontium substitution in cobalt ferrite: structural and optical studies. Mater. Chem. Phys. **272**, 124923 (2021). https://doi.org/10.1016/j.matchemphys.2021.124923
23. N. Rikamukti, P.B. Utari, Effect of doping Strontium ions in co-precipitated cobalt ferrite. J. Phys. Conf. Ser. (2017). https://doi.org/10.1088/1742-6596/909/1/012012
24. A.M. El-Khawaga, M.A. Elsayed, Y.A. Fahim, R.E. Shalaby, Promising photocatalytic and antimicrobial activity of novel capsaicin coated cobalt ferrite nanocatalyst. Sci. Rep. **13**, 5353 (2023). https://doi.org/10.1038/s41598-023-32323-y
25. K. Zarezadeh, S. Sheibani, A. Ataie, Photocatalytic and antibacterial characteristics of decorated polyester textile with ceramic nanoparticles of cobalt ferrite. Ceram. Int. **49**, 20104–20117 (2023). https://doi.org/10.1016/j.ceramint.2023.03.134
26. M. Dhiman, B. Chudasama, V. Kumar et al., Augmenting the photocatalytic performance of cobalt ferrite via change in structural and optical properties with the introduction of different rare earth metal ions. Ceram. Int. **45**, 3698–3709 (2019). https://doi.org/10.1016/j.ceramint.2018.11.033
27. M.A. Abdo, A.A. El-Daly, Sm-substituted copper-cobalt ferrite nanoparticles: preparation and assessment of structural, magnetic and photocatalytic properties for wastewater treatment applications. J. Alloys Compd. **883**, 160796 (2021). https://doi.org/10.1016/j.jallcom.2021.160796
28. S.F. Mansour, F. Al-Hazmi, M.S. AlHammad et al., Enhancing the magnetization, dielectric loss and photocatalytic activity of Co–Cu ferrite nanoparticles via the substitution of rare earth ions. J. Mater. Res. Technol. **15**, 2543–2556 (2021). https://doi.org/10.1016/j.jmrt.2021.09.079
29. G. Bulai, V. Trandafir, S.A. Irimiciuc et al., Influence of rare earth addition in cobalt ferrite thin films obtained by pulsed laser deposition. Ceram. Int. **45**, 20165–20171 (2019). https://doi.org/10.1016/j.ceramint.2019.06.284

30. M.M. Baig, S. Zulfiqar, M.A. Yousuf et al., Structural and photocatalytic properties of new rare earth La3+ substituted MnFe2O4 ferrite nanoparticles. Ceram. Int. **46**, 23208–23217 (2020). https://doi.org/10.1016/j.ceramint.2020.06.103
31. A. Mir, M. Qadeer, R. Waqas, S.N. Khan, Study of morphological, optical and microwave properties of strontium-doped cobalt ferrites. J. Electron Mater. **49**, 4801–4808 (2020). https://doi.org/10.1007/s11664-020-08212-9
32. P. Imanipour, S. Hasani, M. Afshari et al., The effect of divalent ions of zinc and strontium substitution on the structural and magnetic properties on the cobalt site in cobalt ferrite. J. Magn. Magn. Mater. **510**, 166941 (2020). https://doi.org/10.1016/j.jmmm.2020.166941
33. R. Nongjai, S. Khan, K. Asokan et al., Magnetic and electrical properties of in doped cobalt ferrite nanoparticles. J. Appl. Phys. **10**(1063/1), 4759436 (2012)
34. B.K. Lai, A.C. Johnson, H. Xiong, S. Ramanathan, Ultra-thin nanocrystalline lanthanum strontium cobalt ferrite (La0.6Sr0.4Co0.8Fe0.2O3-δ) films synthesis by RF-sputtering and temperature-dependent conductivity studies. J. Power Sour. **186**, 115–122 (2009). https://doi.org/10.1016/j.jpowsour.2008.09.094
35. Y. Yu, K.F. Ludwig, S. Gopalan et al., Surface segregation in strontium doped lanthanum cobalt ferrite: effect of composition and strain. ECS Meet Abstr. (2016). https://doi.org/10.1149/ma2016-02/39/2872
36. J.M. Porras-Vazquez, P.R. Slater, Synthesis of oxyanion-doped barium strontium cobalt ferrites: stabilization of the cubic perovskite and enhancement in conductivity. J. Power Sour. **209**, 180–183 (2012). https://doi.org/10.1016/j.jpowsour.2012.02.105
37. Z. Wang, Z. Yang, Y. Song et al., Alkaline metal doped strontium cobalt ferrite perovskites as cathodes for intermediate-temperature solid oxide fuel cells. Int. J. Hydrogen Energy **43**, 13420–13429 (2018). https://doi.org/10.1016/j.ijhydene.2018.05.057
38. Y.H. Lee, S. Lee, J. Zeng et al., Au-coated lanthanum strontium cobalt ferrite cathode for lowering sheet resistance of a solid oxide fuel cell. Int. J. Precis. Eng. Manuf. **20**, 451–455 (2019). https://doi.org/10.1007/s12541-019-00013-3
39. C. Gómez-Polo, V. Recarte, L. Cervera et al., Tailoring the structural and magnetic properties of Co–Zn nanosized ferrites for hyperthermia applications. J. Magn. Magn. Mater. (2018). https://doi.org/10.1016/j.jmmm.2018.05.051
40. S.B. Somvanshi, S.R. Patade, D.D. Andhare et al., Hyperthermic evaluation of oleic acid coated nano-spinel magnesium ferrite: Enhancement via hydrophobic-to-hydrophilic surface transformation. J. Alloys Compd. **835**, 155422 (2020). https://doi.org/10.1016/j.jallcom.2020.155422
41. D.E.-R. Rayan, M. Ismail, Magnetic properties and induction heating ability studies of spinal ferrite nanoparticles for hyperthermia treatment of tumours. Egypt J. Biomed. Eng. Biophys. (2019). https://doi.org/10.21608/ejbbe.2019.5193.1022
42. B.A. Patil, J.S. Kounsalye, A.V. Humbe, R.D. Kokate, Structural, magnetic, dielectric and hyperfine interaction studies of titanium (Ti4+)-substituted nickel ferrite (Ni1+x-TixFe2−2xO4) nanoparticles. J. Mater. Sci. Mater. Electron **32**, 4556–4567 (2021). https://doi.org/10.1007/s10854-020-05197-3
43. S. Taneja, P. Thakur, R. Kumar et al., Nanostructured rare earth Nd3+doped Nickel–Zinc–Bismuth Spinel Ferrites: structural, electrical and dielectric studies. Ceram. Int. **48**, 27731–27738 (2022). https://doi.org/10.1016/j.ceramint.2022.06.073
44. S.E.M. Ghahfarokhi, M. Ahmadi, I. Kazeminezhad, Effects of Bi3+ substitution on structural, morphological, and magnetic properties of cobalt ferrite nanoparticles. J. Supercond. Nov. Magn. **32**, 3251–3263 (2019). https://doi.org/10.1007/s10948-019-5058-8
45. M. Sumalatha, S. Shravan kumar Reddy, M.S. Reddy et al., Raman and in-field 57Fe Mössbauer study of cation distribution in Ga substituted cobalt ferrite (CoFe2-xGaxO4). J. Alloys Compd. (2020). https://doi.org/10.1016/j.jallcom.2020.155478
46. H. Zhang, Y. Wang, H. Wang et al., Room-temperature magnetoresistive and magnetocaloric effect in La1- xBa xMnO3compounds: Role of Griffiths phase with ferromagnetic metal cluster above Curie temperature. J. Appl. Phys. **10**(1063/5), 0078188 (2022)
47. S. Mimuro, Y. Makinose, N. Matsushita, Low-temperature synthesis of lanthanum strontium cobalt ferrite by the citrate complex method adding oleic acid. Adv. Powder Technol. **26**, 1245–1249 (2015). https://doi.org/10.1016/j.apt.2015.06.006
48. G.D. Han, H.J. Choi, K. Bae et al., Fabrication of lanthanum strontium cobalt ferrite-gadolinium-doped ceria composite cathodes using a low-price inkjet printer. ACS Appl. Mater. Interfaces **9**, 39347–39356 (2017). https://doi.org/10.1021/acsami.7b11462
49. A.T. Le, C.D. Giang, L.T. Tam et al., Enhanced magnetic anisotropy and heating efficiency in multi-functional manganese ferrite/graphene oxide nanostructures. Nanotechnology (2016). https://doi.org/10.1088/0957-4484/27/15/155707
50. S. Sharma, N. Choudhary, M. Kumar Verma et al., Cation distribution and magnetic properties of nano and bulk CoCrFeO4 ferrite synthesized by glycine-nitrate combustion method. Ceram. Int. **43**, 11083–11089 (2017). https://doi.org/10.1016/j.ceramint.2017.05.154

51. S.R. Mokhosi, W. Mdlalose, S. Mngadi et al., Assessing the structural, morphological and magnetic properties of polymer-coated magnesium-doped cobalt ferrite (CoFe2O4) nanoparticles for biomedical application. J. Phys. Conf. Ser. (2019). https://doi.org/10.1088/1742-6596/1310/1/012014
52. A.B. Mugutkar, S.K. Gore, R.S. Mane et al., Magneto-structural behaviour of Gd doped nanocrystalline Co–Zn ferrites governed by domain wall movement and spin rotations. Ceram. Int. **44**, 21675–21683 (2018). https://doi.org/10.1016/j.ceramint.2018.08.255
53. F. Bibi, S. Iqbal, H. Sabeeh et al., Evaluation of structural, dielectric, magnetic and photocatalytic properties of Nd and Cu co-doped barium hexaferrite. Ceram. Int. **47**, 30911–30921 (2021). https://doi.org/10.1016/j.ceramint.2021.07.274
54. V.S. Kirankumar, S. Sumathi, Copper and cerium co-doped cobalt ferrite nanoparticles: structural, morphological, optical, magnetic, and photocatalytic properties. Environ. Sci. Pollut. Res. **26**, 19189–19206 (2019). https://doi.org/10.1007/s11356-019-05286-9
55. N. Ali, A. Said, F. Ali et al., Photocatalytic degradation of congo red dye from aqueous environment using cobalt ferrite nanostructures: development, characterization, and photocatalytic performance. Water Air Soil Pollut. (2020). https://doi.org/10.1007/s11270-020-4410-8
56. A. Amri, K. Hasan, H. Taha et al., Surface structural features and optical analysis of nanostructured Cu-oxide thin film coatings coated via the sol-gel dip coating method. Ceram. Int. **45**, 12888–12894 (2019). https://doi.org/10.1016/j.ceramint.2019.03.213
57. A. Manohar, C. Krishnamoorthi, C. Pavithra, N. Thota, Magnetic hyperthermia and photocatalytic properties of MnFe2O4 nanoparticles synthesized by solvothermal reflux method. J. Supercond. No.v Magn. **34**, 251–259 (2021). https://doi.org/10.1007/s10948-020-05685-x
58. K. Longardner, I. Litvan, J. Wang, Sens. Actuators B Chem. (2021). https://doi.org/10.1016/j.jallcom.2023.170651
59. L. Megatif, R. Dillert, D.W. Bahnemann, Reaction rate study of the photocatalytic degradation of dichloroacetic acid in a black body reactor. Catalysts (2019). https://doi.org/10.3390/catal9080635
60. M. Sun, W. Kong, Y. Zhao et al., Improving photocatalytic degradation activity of organic pollutant by sn4+ doping of anatase tio2 hierarchical nanospheres with dominant 001 facets. Nanomaterials (2019). https://doi.org/10.3390/nano9111603
61. S. Swathi, R. Yuvakkumar, P.S. Kumar et al., Chemosphere Annealing temperature effect on cobalt ferrite nanoparticles for photocatalytic degradation. Chemosphere **281**, 130903 (2021). https://doi.org/10.1016/j.chemosphere.2021.130903